Article

Calcium Sulfate Crystallization in Presence of Fluorecent-Tagged Polyacrylate and Some Refinement of Scale Inhibition Mechanism

Maria Trukhina [1], Sergey Tkachenko [1,2], Anastasia Ryabova [3], Maxim Oshchepkov [2], Anatoly Redchuk [1] and Konstantin Popov [1,*]

[1] JSC "Fine Chemicals R&D Centre", Krasnobogatyrskaya, Str. 42, b 1, Moscow 107258, Russia; truheniy-mv@yandex.ru (M.T.); s.tkach.8@gmail.com (S.T.); aredchuk@gmail.com (A.R.)

[2] Department of Chemistry and Technology of Biomedical Pharmaceuticals, Mendeleev University of Chemical Technology of Russia, Miusskaya sq. 9, Moscow 125047, Russia; maxim.os@mail.ru

[3] Prokhorov General Physics Institute of the Russian Academy of Sciences, Vavilov Str., 38, Moscow 119991, Russia; nastya.ryabova@gmail.com

* Correspondence: ki-popov49@yandex.ru

Abstract: Deposits of calcium sulfate scale on the surfaces of industrial equipment in distillation facilities, reverse osmosis desalination plants, in oil and gas industries lead to significant clogging of pipes and membranes and to a serious increase in production costs. For the mitigation of scale formation, the wide spectrum of antiscalants is applied. The present work is dedicated to the study of calcium sulfate deposition from supersaturated aqueous solutions in the presence of polyacrylic antiscalant with fluorescent marker (naphthalimide fragment) PAA-F1, which provides traceability of the scale inhibitor and a better understanding of its efficacy. A paradoxical phenomenon is being described here. Antiscalant causes a change in the crystal phase from bassanite to gypsum, significantly reduces the amount of deposit, but does not reveal the presence of its molecules either at the kink, step, or at selected edge sites of deposited crystals. Contrary to the predictions of the theory, it either stays in the aqueous phase, or forms its own separate phase Ca-PAA-F1. It is demonstrated that the antiscalant does not block the surfaces of calcium sulfate nuclei or crystal surfaces, but rather the foreign particles of nanodust with particle sizes around 1 nm, naturally occurring in any aqueous solution. As a result, the number of calcium nucleation sites is reduced, and the rate of scale formation decreases without any apparent antiscalant–scale interaction. On the grounds of the current experiment, the substoichiometric effect of scale inhibition obtained an alternative, quite stoichiometric explanation.

Keywords: gypsum; nucleation; scale inhibition; antiscalants; fluorescence; inhibition mechanisms; antiscalant visualization

1. Introduction

Calcium sulfates are among the most common scalants in water desalination plants [1,2], water distillation facilities [3], geothermal power plants [4] and in the oil and gas industry [4,5], causing significant clogging of pipes and membranes and significantly increasing production costs. Depending on the particular conditions, they crystallize as gypsum, calcium sulfate hemihydrate (bassanite), and/or anhydrite [6]. One of the most effective and widely accepted tools to mitigate calcium sulfate scale formation is the use of scale inhibitors [7]. Thus, both the crystallization roots of calcium sulfate deposition from supersaturated aqueous solutions [8–31] and the retardation of scale by various additives [7,32–52] have been the subject of intensive studies over the last 50 years. The former reports consider a wide range of supersaturation degrees [19,20,28], ionic strength values [14,18,26], calcium/sulfate mole ratios [19,24,28], temperatures [11,14,17], and pH values [39], while the latter communications evaluate numerous candidates for calcium sulfate scale inhibition, including various phosphonates [30,38,39,43,45,48,52], polycarboxylates [33,35,37,43,44], chelating agents such

as EDTA [49,50], citric acid [50] and many others for various industrial water treatment technologies, a wide range of antiscalant dosages and different types of scale.

Significant progress has been made since the initial studies of Nancollas [8,11], Packter [9] and Amjad [32,33]. In particular, the originally considered one-step process of gypsum crystallization has been shown to occur via a four-step solution-based nucleation and growth of the $CaSO_4 \cdot 2H_2O$ phase [21]. In a supersaturated aqueous solution, the reaction between Ca^{2+} and SO_4^{2-} ions begins with the rapid formation of primary solid species about c.a. 3 nm in length (first step), followed by their arrangement into domains in the second step, which self-assemble into large aggregates in the third step. Within the aggregates, these well-defined primary species begin to grow (step four), and through structural rearrangement crystallize into gypsum. At the same time, different intermediate phases are expected to form as precursors to gypsum: amorphous calcium sulfate and/or nanocrystalline bassanite [21,51]. Depending on the supersaturation degree, the first stage in the bulk solution is treated as either a heterogeneous or as homogeneous process [53,54]. The latter mechanism assumes the spontaneous association of calcium and sulfate ions into solid nano-aggregates, while the former one is induced by the presence of foreign surfaces such as dust particles, bubbles, or foreign molecules.

Recent views on the role of antiscalants [55] admit that they can affect any of the aforementioned steps of gypsum crystallization. There is a general agreement that scale inhibitors can act in a bulk aqueous medium by several possible routes simultaneously [6,7,34,45,55,56]. They can: (i) increase scale solubility by masking calcium cations via formation of soluble complexes; (ii) adsorb onto sparingly soluble salt nuclei (this reduces the rate at which nuclei cross the critical size barrier, the "threshold effect", and thus reduces the rate of scale nucleation); (iii) adsorb onto dust particles and isolate them from calcium and sulfate ions (this also reduces the number of nucleation sites); (iv) impart a significant electrostatic charge to the scale nuclei, retarding their aggregation by electrostatic repulsion between sparingly soluble salt colloids; and (v) adsorb onto growing crystals and block the crystal growth centers (sometimes changing the crystal habit and slowing further crystal growth). However, the relative contribution of each mechanism in specific cases (evaporation, reverse osmosis, oilfield facilities, etc.) is usually unclear.

Meanwhile, the uncertainty can be eliminated by the application of fluorescent-tagged antiscalants [56–64]. Indeed, the visualization of phosphonates and polyacrylates during gypsum crystallization in a series of experiments within 2019–2023 provided unique information that contradicted the conventional theory of scale inhibition. Already the first communication, focusing on the localization of the fluorescent-tagged bisphosphonate HEDP-F (1-hydroxy-7-(6-methoxy-1,3-dioxo-1H-benzo[de]isoquinolin-2(3H)-yl)heptane-1,1-diyldi(phosphonic acid)) localization during gypsum deposition [58] described a paradoxical effect. It was found that, contrary to the popular belief, HEDP-F does not interact at all with $CaSO_4 \cdot 2H_2O$ crystals at ambient temperature, but does retard, nevertheless, gypsum scaling from supersaturated solution in a batch test. In this study, the antiscalant formed its own separate solid phase Ca-HEDP-F, while the gypsum crystals showed no traces of scale inhibitor on their surface.

Later, the similar phenomenon was independently reported for both static and dynamic conditions of gypsum crystallization at ambient temperature in the presence of HEDP-F [59,60] and fluorescent-tagged polyacrylate PAA-F1 [60]. This effect has been explained in terms of "antiscalant—solid nanoimpurities" interactions [56,58]. At the same time, it was noted that, in a static test, performed according to NACE recommendations TM0374-2007 (24 h heating of supersaturated gypsum solution at 70 °C), HEDP-F was found both inside and on the surface of $CaSO_4 \cdot 2H_2O$ crystals [58]. Thus, the mechanisms of gypsum scale inhibition at ambient and elevated temperatures appear to be different.

Polycarboxylates are known to be effective scale inhibitors for calcium sulfate scale deposits [33,35,37,43,44]. In order to gain further fundamental understanding of gypsum

crystallization in the presence of polymers and of the inhibition mechanisms, it is of particular interest to use fluorescently labeled reagents to highlight their actual location. The key objectives of the present study are: (i) to evaluate the efficacy of the fluorescent-tagged polyacrylate PAA-F1 [64], Figure 1, at different supersaturation levels in a static batch experiment, and (ii) to gain insight into the inhibition mechanisms by visualizing the scale inhibitor by controlling it in both aqueous and solid phases.
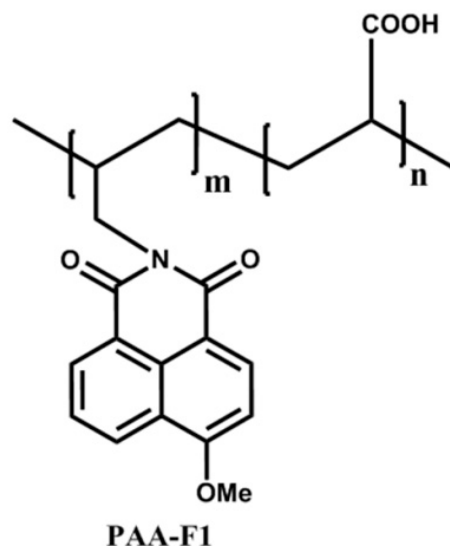

Figure 1. Molecular structure of naphthalimide-tagged polyacrylate PAA-F1.

2. Materials and Methods

2.1. Materials

Deionized water and reagent-grade quality chemicals were used for the preparation of calcium chloride and sodium sulfate stock solutions. $CaCl_2$ solution was prepared from $CaCO_3$ (GOST 8253-79, 99.0%) with HCl (GOST 14261-77, p.p.s. 20-4, 37%). Na_2SO_4 (GOST 21458-75, RU; 98.94%) and in-house deionized water (DI water; Laboratory Reagent Water Type I, ASTM D1193-06(2011), 0.056 μS/cm) was used in the current study for the preparation of gypsum stock solutions. The water passed a preliminary analysis by a particle counter technique before use (Table 1). These data show that an in-house deionized water complies well with the international standards and does not affect the natural level of foreign particle content, contributed by $CaCl_2$ and Na_2SO_4. Most of particulate matter is therefore introduced by $CaCl_2$ and Na_2SO_4 and increases with SI growth, Table 1.

Table 1. Characteristics of the Blank experiments I, III and V.

Sample	$[Ca]_{init}$, $mol \cdot dm^{-3}$	$[Ca]_{fin}$, $mol \cdot dm^{-3}$	$[CaSO_4]_{init}$, %	SI	Cumulative Initial Particle Concentration, Units per 1 mL			pH	Crystal Form of Sediment
					>100 nm	>200 nm	>300 nm		
DI water	-	-	-	-	1290 ± 20	89 ± 5	41 ± 4	5.65	-
I	0.13	0.030	50	4.3	4760 ± 150	3720 ± 150	2470 ± 130	6.6	100% $CaSO_4 \cdot 0.5H_2O$
III	0.07	0.024	45	3.0	2560 ± 130	2000 ± 130	1330 ± 300	6.4	100% $CaSO_4 \cdot 0.5H_2O$
V	0.05	0.023	32	2.2	1830 ± 120	1430 ± 100	950 ± 90	6.1	100% $CaSO_4 \cdot 0.5H_2O$

Naphthalimide-tagged polyacrylate PAA-F1 was synthesized by our group as described elsewhere [64]. It has molecular mass of 4000 Da, and the naphthalimide moiety constitutes 0.5 mass %.

2.2. Scale Formation Procedure

The modified static batch NACE test [65] was used in the present work: no background NaCl was added, and the supersaturation degree was variable, varying from 2.2 to 4.3. The stock solutions of $CaCl_2$ (10.5% mass) and Na_2SO_4 (10.0% mass) were prepared and filtered before use (450 nm; mixed cellulose ester membrane filters, Whatman GmbH). Then, a set of five blank supersaturated gypsum solutions with 1:1 calcium/sulfate mole ratio and initial calcium sulfate concentrations of 0.125 (sample I), 0.086 (sample II), 0.070 (sample III), 0.063 (sample IV) and 0.049 (sample V) $mol \cdot dm^{-3}$ was prepared, heated at 70 ± 1 °C for 24 h, and then cooled to 25 °C. An aliquot of the resulting solution was filtered (blue ribbon filter paper) and analyzed by a standard EDTA titration procedure for the residual calcium content in the aqueous phase. The supersaturation degree (SI) was calculated as the ratio of the initial calcium concentration ($[Ca]_{init}$, $mol \cdot dm^{-3}$) to the final concentration ($[Ca]_{fin}$, $mol \cdot dm^{-3}$) in the blank run: $SI = [Ca]_{init}/[Ca]_{fin}$. Thus, the following SI values were studied: 4.3 (I), 3.6 (II), 3.0 (III), 2.6 (IV) and 2.2 (V). In parallel, the % of $[CaSO_4]$ complexes was calculated for each particular SI value using the SPECIES software [65] and corresponding stability constants, Table 1. The sediments were isolated, dried and examined by scanning electron microscopy (SEM) and X-ray diffraction (XRD). The cumulative data from the blank experiments are presented in Table 1.

In the same way a series of five experiments Ia-Va was carried out in the presence of 10 $mg \cdot dm^{-3}$ of PAA-F1, Table 2. In all cases, PAA-F1 was primarily added to the Na_2SO_4 solution. The sediments were isolated, dried and examined by SEM and XRD. In parallel, the isolated liquid phase was analyzed by spectrofluorimetry for the residual PAA-F1 content and by EDTA titration for residual calcium concentration. In addition, the liquid samples in equilibrium with the sediment, if any, were collected and analyzed by confocal luminescence microscopy (FM) the next day after each experiment. An antiscalant efficacy (*AE*) was estimated according to Equation (1):

$$AE = \frac{C_{Ca}{}^{ing} - C_{Ca}{}^{blank}}{C_{Ca}{}^{total} - C_{Ca}{}^{blank}} \cdot 100 \tag{1}$$

where $C_{Ca}{}^{total}$ is the initial concentration of calcium in the aqueous phase, $mg \cdot dm^{-3}$, $C_{Ca}{}^{ing}$ is the final concentration of calcium in the aqueous phase in the presence of the antiscalant, $mg \cdot dm^{-3}$, and $C_{Ca}{}^{blank}$ is the final concentration of calcium in the aqueous phase in the corresponding blank experiment, $mg \cdot dm^{-3}$.

Table 2. Results of experiments, performed in the in presence of 10 $mg \cdot dm^{-3}$ PAA-F1.

Sample	$[Ca]_{init}$, $mol \cdot dm^{-3}$	$[Ca]_{fin}$, $mol \cdot dm^{-3}$	SI	pH	AE, %	$[PAA-F1]_{init}$, $mg \cdot dm^{-3}$	$[PAA-F1]_{final}$, $mg \cdot dm^{-3}$	Residual PAA-F1 in Aqueous Phase, %	Crystal Form of Sediment
Ia	0.125	0.031	4.3	6.5	2.2 ± 0.4	10.2 ± 0.1	6.8 ± 0.2	67 ± 2	100% $CaSO_4 \cdot 2H_2O$
IIa	0.086	0.034	3.6	6.1	16.3 ± 0.8	10.4 ± 0.1	7.8 ± 0.2	75 ± 1	100% $CaSO_4 \cdot 2H_2O$
IIIa	0.070	0.044	3.0	6.2	42 ± 1	10.3 ± 0.1	9.4 ± 0.3	88 ± 2	100% $CaSO_4 \cdot 2H_2O$
IVa	0.063	0.059	2.6	6.1	88 ± 4	10.3 ± 0.1	9.4 ± 0.1	92 ± 1	Due to high AE, no sediment found, suitable for XRD analysis
Va	0.049	0.049	2.2	6.1	99.5 ± 0.5	10.2 ± 0.1	10.0 ± 0.2	98 ± 2	

2.3. Liquid and Solid Phase Characterization Methods

After separation, rinsing and air drying at 50 °C, the precipitated solids were characterized by SEM (Hitachi TM-3030, Tokyo, Japan) and powder XRD (Bruker D8 Advance diffractometer; Cu KD; Ni-filter; LYNXEYE detector, Billerica, MA, USA). XRD phase identification was performed using the Joint Committee on Powder Diffraction Standards (JCPDS) database, and relative phase content was estimated using Topaz

R software (Bruker AXS). Sample examinations by SEM were performed at 15 kV accelerating voltage in a charge-up reduction mode with the crystal phase placed on a double-sided conductive tape.

Fluorescence microscopy (FM) measurements were performed with a laser scanning confocal microscope LSM-710-NLO (Carl Zeiss Microscopy, Jena, Germany), with a $\times$20 Plan-Apochromat objective (NA = 0.8) for both liquid and solid samples. Antiscalant fluorescence was recorded in the 470–600 nm wavelength range, when excited by a 458 nm laser. The liquid samples were placed on the Petri dish with a glass bottom 0.16 mm thick and are presented as 2D images. Although PAA-F1 exhibits fluorescence in the blue region of the spectrum, the fluorescence channel was assigned the green pseudocolor because the dynamic range of human color perception for green is much wider than for blue. Thus, in our report, the original blue emission of PAA-F1 is altered for an artificial green pseudocolor.

The mass concentration of PAA-F1 in the test solutions was measured by spectrofluorimetric analysis (Shimadzu RF-6000 (Shimadzu, Kyoto, Japan) spectrofluorimeter) in 10 mm cuvettes. The fluorescence intensity of the solution was registered at 460 nm, using an excitation wavelength of 375 nm. To establish the calibration curve for a mass concentration range of PAA-F1 between 0.5 and 15 mg·dm^{-3}, six solutions with concentrations of 0.5, 1.0, 2.5, 5.0, 10.0 and 15.0 mg·dm^{-3} were prepared from the stock solution of PAA-F1. The solutions were analyzed immediately after preparation. The fluorescence intensity of the solution was measured at 460 nm. The calibration curve is plotted in the coordinates "fluorescence intensity—mass concentration of PAA-F1" (mg·dm^{-3}). The slope is described by the function y = a·x. The calibration response is fitted by the method of least squares.

The SLS-1100 particle counter (Particle Measuring Systems Inc., Boulder, CO, USA) was used to quantitatively characterize the suspended solid contaminant concentration of the particles sized $\geq$100 nm in stock solutions. This instrument provides a particle concentration measurement in the size range from 100 nm to 1 mm. Due to the high concentration of particles in the filtered solutions, the corresponding stock solution probe was diluted 100-fold with deionized water, the measurement was performed, and the results were recalculated back to the initial concentration. For gypsum solutions, direct experimental measurements were not performed because the measurement time was comparable to the nucleation time. Therefore, the nano-/microparticle concentration at the moment of mixing of calcium and sulfate brines was taken as an average value for the corresponding stock solutions, Table 1 (Cumulative Initial Particle Concentration).

The liquid phase was monitored by dynamic light scattering technique (DLS) for qualitative characterization of suspended solid contaminants within the particles size (hydrodynamic diameter) range of 1 to 1000 nm. DLS measurements of sulfate and calcium stock solutions were performed using the dynamic light scattering technique at 25 °C with a Malvern Nano ZS instrument, Malvern Instruments Ltd., Worcestershire, UK (λ = 633 nm, operating power 4 mW) at Θ = 173°. The results are presented in Table 3. In addition, the size of the polymer itself (PAA-F1 particles) was measured with this technique in DI water and in CaCl$_2$ solutions at two different pH values, Table 4.

Table 3. DLS analysis of sodium sulfate and calcium chloride concentrates.

Aqueous Solution Studied	Solution Concentration, mol·dm^{-3}	Fractions Distribution by Number		Fractions Distribution by Intensity	
		Mean Size, nm	Relative Content, %	Mean Size, nm	Relative Content, %
Na$_2$SO$_4$	0.07	0.8 ± 0.2	100	1.0 ± 0.2 160 ± 40	13 ± 5 87 ± 5
CaCl$_2$	0.09	0.7 ± 0.2	100	1.0 ± 0.2 400 ± 40	10 ± 7 90 ± 7

Table 4. DLS analysis of 10 mg·dm^{-3} PAA-F1 solutions.

Sample	pH	Fractions Distribution by Number		Fractions Distribution by Intensity	
		Mean Size, nm	Relative Content, %	Mean Size, nm	Relative Content, %
PAA-F1 in DI water	4.0	380 ± 60	100	280 ± 50	100
	7.0	270 ± 50	100	280 ± 40	100
PAA-F1 in 0.07 mol·dm^{-3} CaCl$_2$ solution [a]	4.0	440 ± 170	100	530 ± 190	100
	7.0	420 ± 150	100	500 ± 160	100
PAA-F1 in 0.125 mol·dm^{-3} CaCl$_2$ solution [b]	4.0	480 ± 110	100	510 ± 110	100
	7.0	380 ± 120	100	430 ± 120	100

[a] Corresponds to calcium content in III and IIIa samples; [b] Corresponds to calcium content in I and Ia samples.

Chemical equilibrium modeling was performed using SPECIES software [66] and a set of stability constants [67]. Among these, the random calcium complex formation constant with sulfate ion [29] logK_{CaL} = 1.3, was taken for 25 °C and ionic strength I = 0.1–0.2 mol·dm^{-3}. This provided an estimate of the percentage of [CaSO$_4$]^0 species in the total calcium content at the moment, when the calcium and sulfate solutions are mixed. The results are presented in Table 1.

A mean distance between the smallest solid impurities with sizes around 1 nm in stock concentrates of 0.07 Na$_2$SO$_4$ mol·dm^{-3} and 0.09 mol·dm^{-3} CaCl$_2$ solutions was estimated on the basis of probability theory [68] using the online calculator Wolfram Alpha [69]. The procedure is described in a SUPPLEMENT.

3. Results

3.1. DLS Studies of PAA-F1 Solutions

The DLS data, presented in Table 4, demonstrate that PAA-F1 molecules form stable aggregates with a mean hydrodynamic diameter between 300 and 500 nm. Meanwhile, a single molecule of polyacrylate with molecular mass of 4000 Da has a length of no more than c.a. 12–13 nm if it has a fully stretched configuration. Thus, the observed size of PAA-F1 particles should correspond to aggregates of a rather large number of macromolecules. In particular, the size of these aggregates is not affected by pH variation, or by the presence of calcium ions: the corresponding changes do not exceed the experimental errors of the mean size measurements with the DLS technique. The formation of calcium complexes with PAA-F1 in aqueous solution cannot be excluded, as a separate phase Ca-PAA-F1 was detected in this work, and in our previous studies [60]. However, the chelating fragments of each polyacrylate (-CH$_2$CH(COOH)CH$_2$CH(COOH)- and (-CH$_2$CH(COOH)CH(COOH)CH$_2$-) can only form eight- or seven-membered cycles with calcium ions, respectively. Such complexes do not exhibit high thermodynamic stability. The corresponding formation constants (logK_{CaL}) of calcium complexes with a low molecular weight analog (succinic acid) at 25 °C are in the range of 1.0 to 2.0 [67]. A complex formation model of 0.135 mmol·dm^{-3} of succinic acid (H$_2$L) complexing with 50 mmol·dm^{-3} of Ca^{2+}, using SPECIES software [66] for 0.1 mol·dm^{-3} ionic strength, 25 °C and logK_{CaL} = 1.15, logK_{HL} = 5.25 and logβ_{H2L} = 9.27 gives 37% of L binding with calcium at pH = 6 and 40% binding at pH = 6.5. Therefore, antiscalants in Na$_2$SO$_4$ solutions initially represent rather stable and probably loose aggregates of PAA-F1 molecules with an average size of 300 nm, which become partially saturated with calcium ions when CaCl$_2$ solution is added.

3.2. Blank Experiments

The blank experiments revealed rather fast formation of deposits in the form of needle-like crystals of calcium sulfate hemihydrate (bassanite) in the whole range of SI used, Figure 2. It is noteworthy that the values of [Ca]$_{fin}$ increase steadily from 0.023 to 0.029 mol·dm^{-3} as the SI increases from 2.2 to 4.3, Table 1. This is in good agree-

ment with the well-known fact that calcium sulfate solubility increases with increasing ionic strength, provided by Na^+ and Cl^- ions [70].
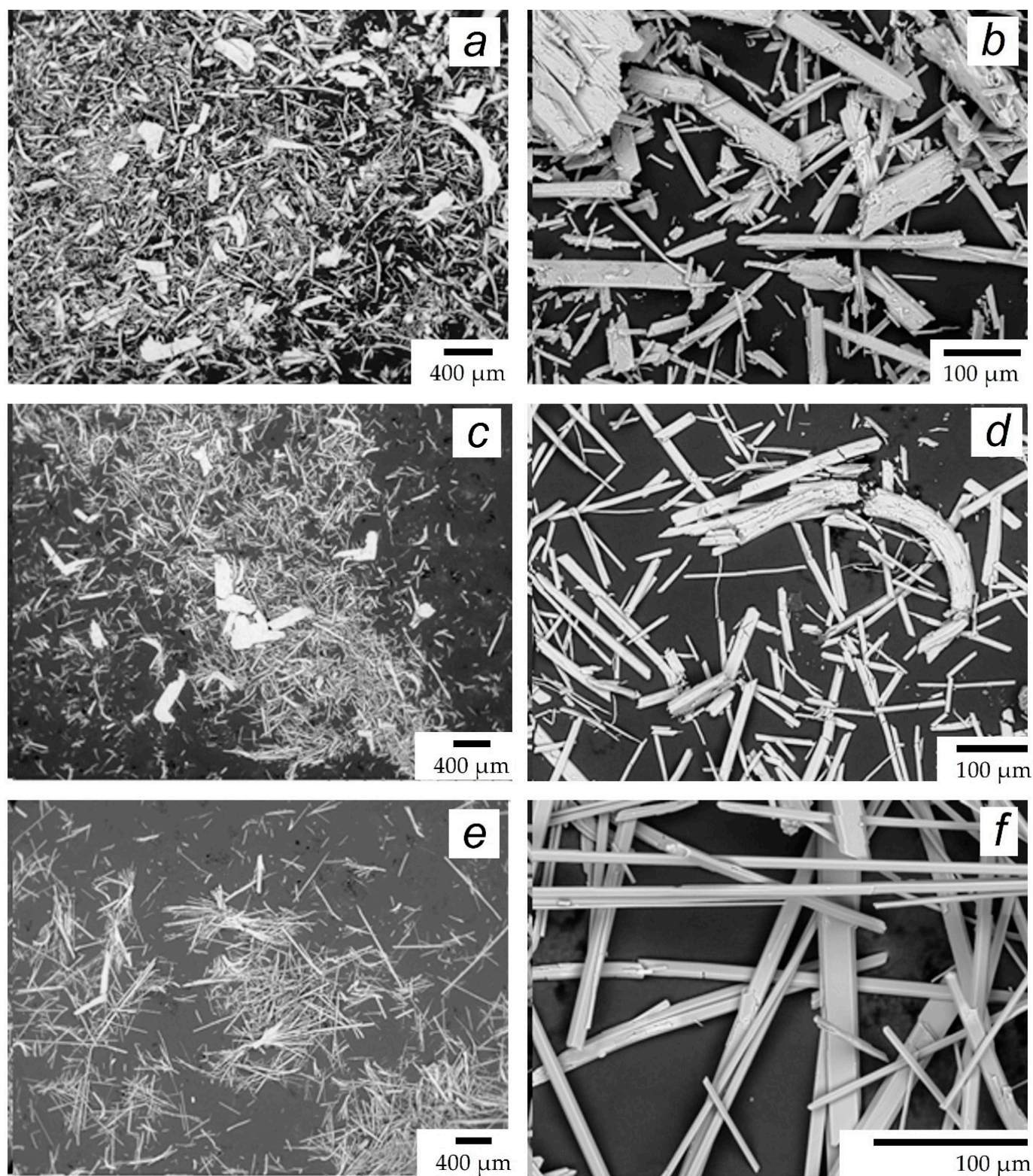

Figure 2. SEM images of calcium sulfate crystals, isolated from I (**a**,**b**), III (**c**,**d**), and V (**e**,**f**) samples from blank experiments.

3.3. Experiments with PAA-F1

The application of the antiscalant PAA-F1 leads to the drastic changes in the crystal form of the sediment and in the rate of its formation, Table 2. Instead of bassanite, gypsum crystals with a completely different morphology are formed, Figure 3. At the same time, PAA-F1 shows a high efficacy in gypsum scale inhibition, Table 2, which steadily decreases from 99 to 2% as SI increases. Both effects are well known for polyacrylates [6,33,35,37,55]. However, the unique ability to track the location of the scale inhibitor due to the implemented fluorescent fragment indicates a paradoxical phenomenon, which contradicts conventional views of scale inhibition mechanisms [56,56,63].
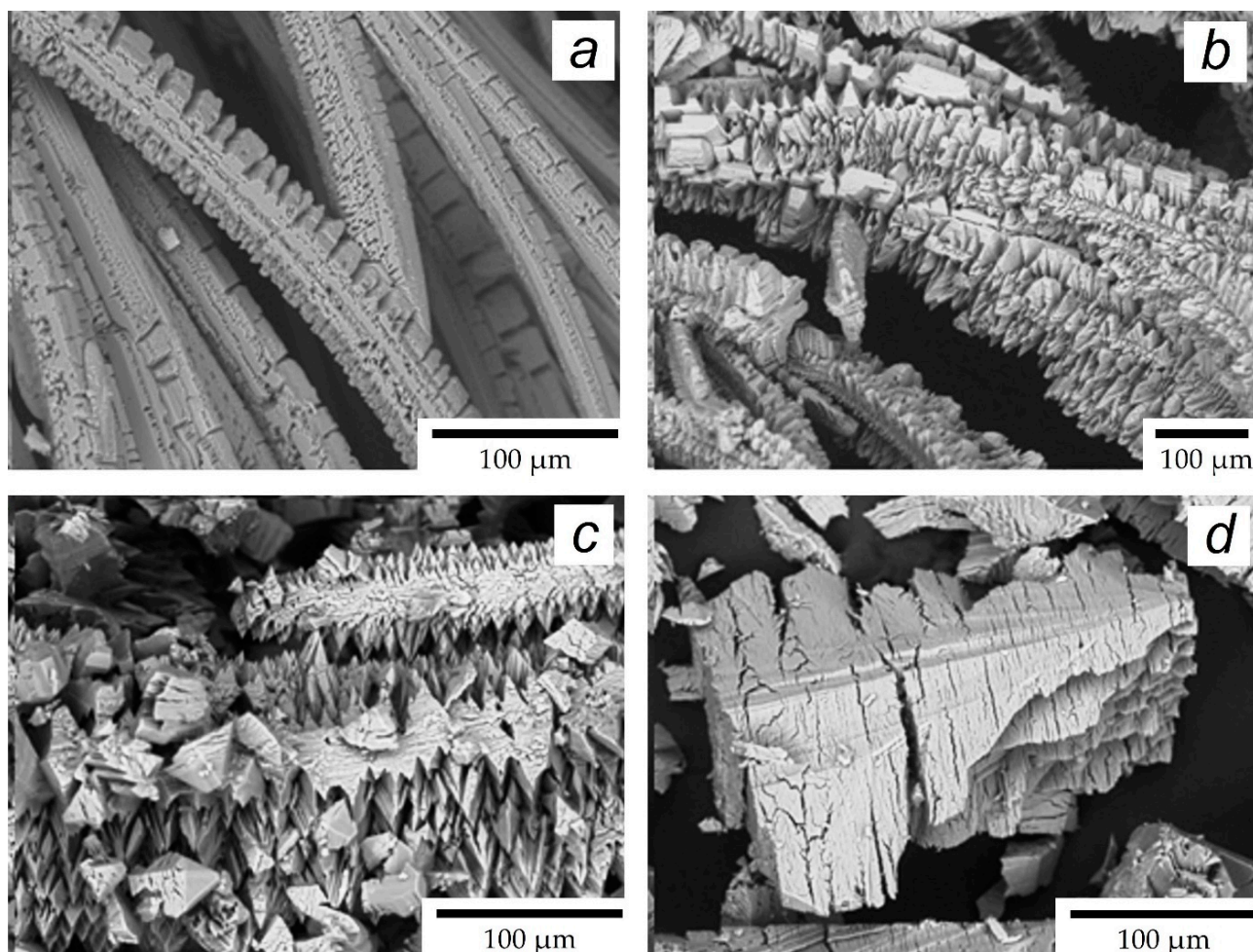

Figure 3. SEM images of calcium sulfate crystals, isolated from Ia (**a**), IIa (**b**), IIIa (**c**) and IVa (**d**) samples of experiments, performed in the presence of 10 mg·dm^{-3} PAA-F1.

First of all, the most astonishing result is related to the absence of antiscalant on the surface or inside the gypsum crystals. This follows from the two independent observations. Fluorescence is not found at the kink, step, or selected edges of gypsum crystals, Figure 4. Only a few traces of PAA-F1 can be observed on the surface of macrocrystals, Figure 4d. On the rest of the images, the fluorescence is concentrated in tiny spherical particles, which we assigned to the separate Ca-PAA-F1 phase based on our previous work with a similar reagent PAA-F2 [60]. This can be clearly seen in the images "a" and "b", Figure 4. This observation is supported by the independent measurements of the PAA-F1 concentration in the aqueous phase, Table 2. In fact, in all our experiments, most of the antiscalant mass (from 67 to 98%) remains in the aqueous phase. The most striking result is related to the Ia sample. In this experiment, when it seems that the antiscalant is not able to provide inhibition in a high excess of calcium sulfate, and should be completely consumed by the

gypsum phase at least in the form of an adsorption layer on $CaSO_4 \cdot 2H_2O$ crystals, 67% of PAA-F1 remains in solution, and the remaining 37% are concentrated in their own phase Ca-PAA-F1. Thus, contrary to the popular belief, the change in the morphology of calcium sulfate cannot be explained by the direct interaction of the antiscalant with calcium.
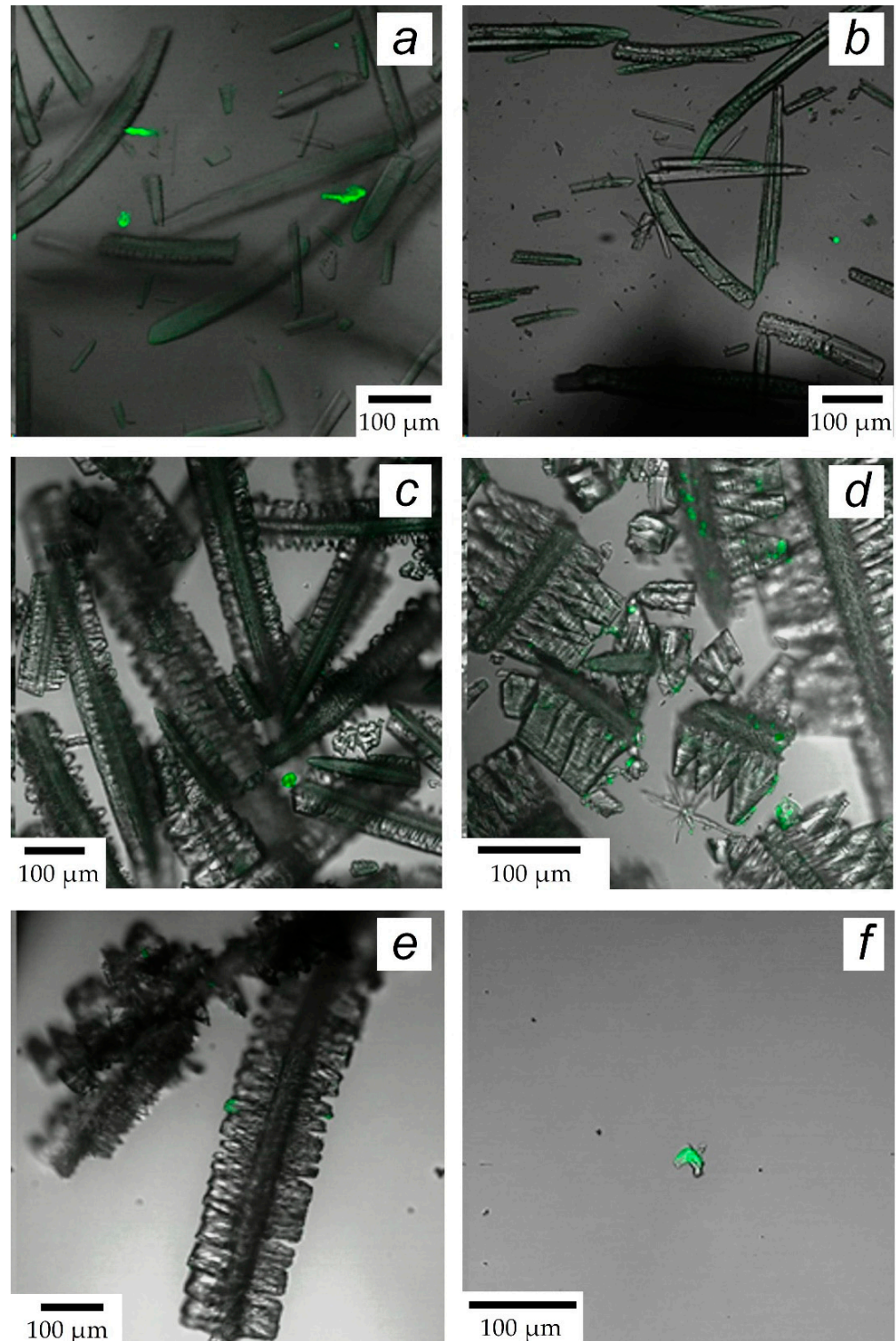

Figure 4. Two-dimensional images of calcium sulfate crystals in equilibrium with mother liquor in the presence 10 mg·dm^{-3} of PAA-F1 in Ia (**a**,**b**), IIa (**c**), IIIa (**d**), Va (**e**) and Va (**f**) samples. The green color indicates location of PAA-F1.

Another paradox is related to the substoichiometric effect. In our experiments, the molar concentration of calcium sulfate changes from 0.05 to 0.13 $mol \cdot dm^{-3}$, while the corresponding solubilities at 25 °C are 0.023 and 0.030 $mol \cdot dm^{-3}$, respectively. Thus, in the case of the Va sample, 10 $mg \cdot dm^{-3}$ PAA-F1, which provides 98% inhibition, should retain 0.027 $mol \cdot dm^{-3}$ in the aqueous phase. The molecular mass of the major chelating fragment of PAA-F1 ($-CH_2CH(COOH)CH_2CH(COOH)-$) corresponds to 144 Da. Thus, 10 $mg \cdot dm^{-3}$ of PAA-F1 contains approximately 0.07 $mmol \cdot dm^{-3}$ of such fragments (the presence of 0.5% mass of fluorescent fragment in PAA-F1 molecule can be neglected). This means that about 0.07 mmol of such chelating fragments must somehow interact with at least 0.027 mol of calcium sulfate species (Ca^{2+}, SO_4^{2-}, $[CaSO_4]^0$) to keep them from forming a solid phase. However, the molar ratio [calcium sulfate species]/[chelating agent fragments of PAA-F1] ~3900 makes it impossible for the antiscalant to prevent deposit formation by sequestration. Such a mechanism is definitely not possible.

Meanwhile, this situation is complicated by the fact that these chelating fragments are concentrated in aggregates of macromolecules that have c.a. 300 nm average diameter, Table 4. A significant part of carboxyl groups seems to be inside this aggregate, and is hardly available for contacts with calcium ions, or with $[CaSO_4]^0$ species. On the other hand, such aggregates have low mobility and are not able to provide a "threshold effect", e.g., to adsorb on the spontaneously forming nuclei of calcium sulfate solids, and not to let them grow beyond the critical size, or to form some nuclei, isolating gypsum nuclei from the bulk solution, Figure 5. This has been a very common opinion recently [6,44,55,71–73]. Likewise, it is extremely unlikely that PAA-F1 can stabilize gypsum nuclei by electrostatic repulsion. We have shown that under similar conditions, gypsum solids have zeta potentials much lower than that required for electrostatic stabilization [43].
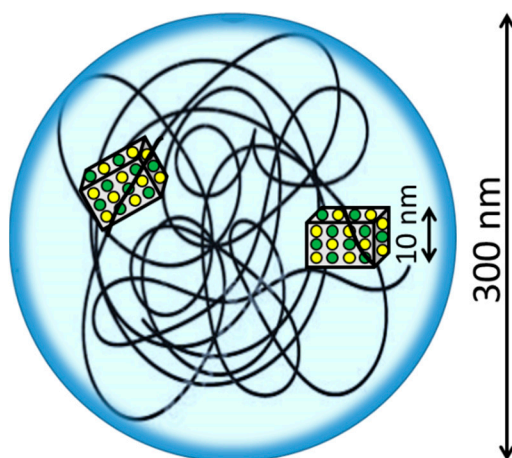

Figure 5. A widely accepted, but unrealistic scheme of gypsum scale inhibition by polyacrylates; yellow and green circles correspond to calcium and sulfate ions, respectively.

Thus, our results do not fit any of the generally accepted mechanisms mentioned in the Introduction section with the exception of antiscalant sorption on dust particles, which occurs naturally in any aqueous solution. To our knowledge, this is the only mechanism that provides a consistent explanation for all our observations.

4. Discussion

4.1. Mechanism of Calcium Sulfate Nucleation in Bulk Solutions

A precise quantitative determination of all solid impurities with sizes above 1 nm is hardly possible nowadays. For semi-quantitative estimation, we have used a combination of particle counter (quantitative measurement of particles with diameter > 100 nm), Table 1, and a relative abundance of different fractions, provided by the DLS technique, Table 3. Sample I was selected for particulate matter assessment because it provided

the most reproducible DLS results. The mean concentration of foreign particles larger than 100 nm in the 1:1 volume mixture of stock solutions of Sample I is estimated to be approximately 5000 units per 1 mL, or 5×10^6 units per 1 dm^3. However, all these particles are not detected in DLS mode registration by number. Only one stable band is detected, related to the fraction of approximately 1 nm, Table 3. This indicates, that the concentration of this fraction in number of particles per 1 mL is much higher than that one of sizes >100 nm. Meanwhile, in the registration mode by intensity the light scattering bants for 1 nm and 160–400 nm fractions become comparable, with the latter dominating, Table 3. Then, for simplicity we make some assumptions: (i) all particles are spherical; (ii) there are only two fractions in the system with mean sizes of 1 and 100 nm; (iii) the concentration of the second one is known and corresponds to 5000 units per 1 mL; (iv) a relative light scattering intesity of 1 and 100 nm light scattering bands in intensity mode is equal. Thus, using the Rayleigh scattering law (the scattering is proportional to the radius to the sixth power), it is possible to calculate the concentration of particles, belonging to the 1 nm fraction: approximately $5 \cdot 10^{15}$ units per 1 mL. This means, that in any cubic volume of the bulk solution with a 100 nm edge there would be an average of five particles with a hydrodynamic diameter of 1 nm. As a next step, we calculated the distribution of such particles in the bulk solution, SUPPLEMENT. The average distance between the particles was found to be about 32 nm. Thus, the longest distance from any calcium sulfate species (Ca^{2+}, SO$_4^{2-}$, [CaSO$_4$]^0) to soilid impurity would not exceed 16 nm. Therefore, the solid crystallization centers are within "walking distance" for any ionic and molecular species of gypsum.

It is then quite natural that the solid impurities would serve as centers of heterogeneous bulk nucleation of calcium sulfate, Figure 6. This figure presents the proposed scheme of such nucleation with the actual scale of the dimensions in the drawing: the red sphere corresponds to the idealized nanoimpurity particle with a diameter of 1 nm, while the yellow and green spheres symbolize Ca^{2+} and SO$_4^{2-}$ ions, respectively. The associated yellow and green spheres represent [CaSO$_4$]^0 complexes. Obviously, any solid impurity particle is capable of adsorbing several [CaSO$_4$]^0 and/or Ca^{2+} species, and initiating the further formation of calcium sulfate nuclei. Such a scheme is in good agreement with the heterogeneous mechanism of the bulk nucleation of sediments [53,54], which is energetically much more favorable than the spontaneous homogeneous one. In our opinion, it is the most realistic and well-founded explanation for our experiments.
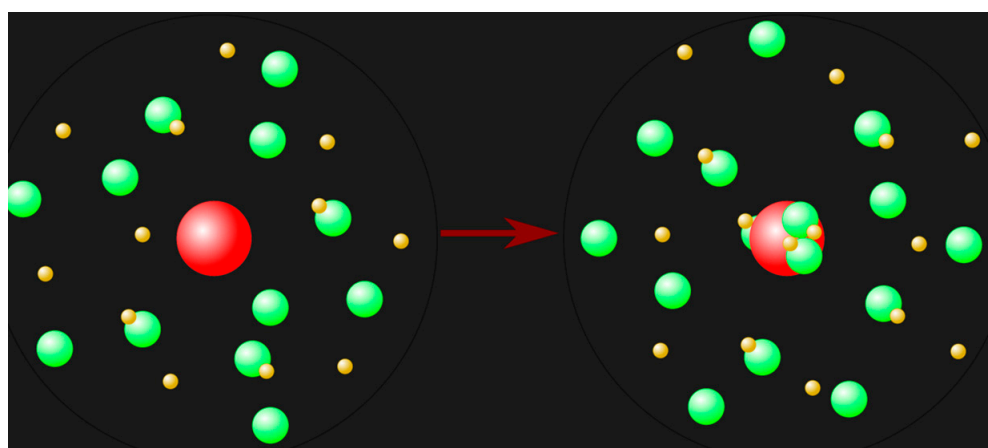

Figure 6. The proposed scheme of calcium sulfate nucleation by nanodust particles (red spheres); green spheres correspond to sulfate ions, yellow spheres—to calcium cations.

4.2. Mechanism of Calcium Sulfate Sulfate Scale Inhibition by PAA-F1 in Bulk Solutions

The only scheme that can explain all of the above paradoxes is shown in Figure 7. This scheme assumes that the antiscalant does not block the surfaces of calcium sulfate nuclei or crystal surfaces, but rather the foreign particles of nanodust. In terms of the large

aggregates of PAA-F1 molecules, the scheme is as shown in Figure 8: the PAA-F1 aggregate accumulates particulate matter. Then, the number of calcium nucleation centers available for gypsum crystal nucleation is reduced, and the rate of scale formation decreases. At the same time, under the high excess of calcium ions, the nanodust saturated aggregates of PAA-F1 form their own Ca-PAA-F1 phase, Figure 9. An estimated accumulation of foreign nanoparticles in Ca-PAA-F1 crystal is shown in the scheme, presented in the right part of Figure 8. Nanodust species are enlarged tenfold for better visibility. Thus, according to the proposed scheme, PAA-F1 can provide scale inhibition without any direct interaction with either the scale-forming ingredients or with the scale surface. It fits well with the heterogeneous bulk nucleation pathway [53,54]. On the other hand, an idea of nanodust accumulation by the aggregates of PAA-F1 molecules is in good agreement with reports of efficient heat transfer surface fouling mitigation by the wood pulp fibers and synthetic fiber suspensions [74,75], which could also be responsible for nanodust accumulation. At the same time, the current study provides further confirmation of our recent results on the key role of particulate matter in calcium sulfate nucleation [76] and in the suppression of antiscalant activity [77].
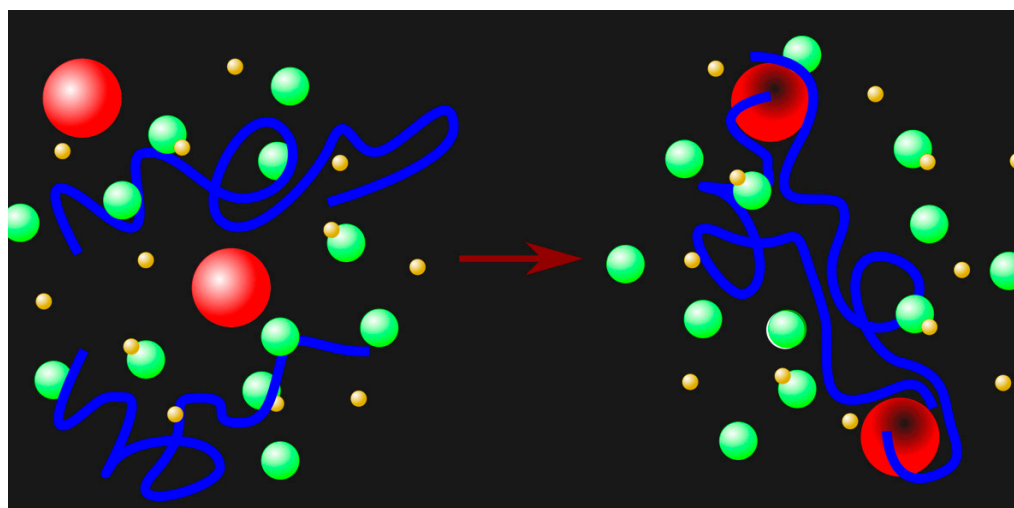

Figure 7. The possible idealized scheme of solid impurities (red spheres) being blocked by PAA-F1 molecules (blue ribbon); green spheres correspond to sulfate ions, yellow spheres—to calcium cations.

The heterogeneous mechanisms of scale formation and scale inhibition in the bulk aqueous medium have recently been gaining wider acceptance [29,36,57]. Unfortunately, the issues of the chemical nature of nanoimpurities and their variability from sample to sample have been little studied [78]. One possible type of such solid impurity may be calcium carbonate as a component of the $CaCl_2$ reagent. Recent crystallographic studies [79,80] report that calcite can provide a good background for calcium sulfate deposition on its surface. It is then reasonable to assume that something similar could happen at the nanoscale level. In any case, much work remains to be conducted in this area.

At the same time, shifting the focus of inhibition from "scale—antiscalant" to "antiscalant—nanodust" interaction eliminates the problem of substoichiometry. In fact, $10 \text{ mg} \cdot \text{dm}^{-3}$ of PAA-F1 with a molecular mass of 4000 Da corresponds to 2.4×10^{18} molecules in one dm^{-3} with a size of about 12 nm. On the other hand, the concentration of 1 nm nanodust particles in our case is 5×10^{18} units per one dm^{-3}. This means that the particle/antiscalant ratio is 1:2. A single molecule of PAA-F1 is not able to bind 10^5 calcium ions, but it is quite capable of isolating 2 nanodust particles from these calcium ions. Thus, the substoichiometric effect gets quite a stoichiometric explanation.
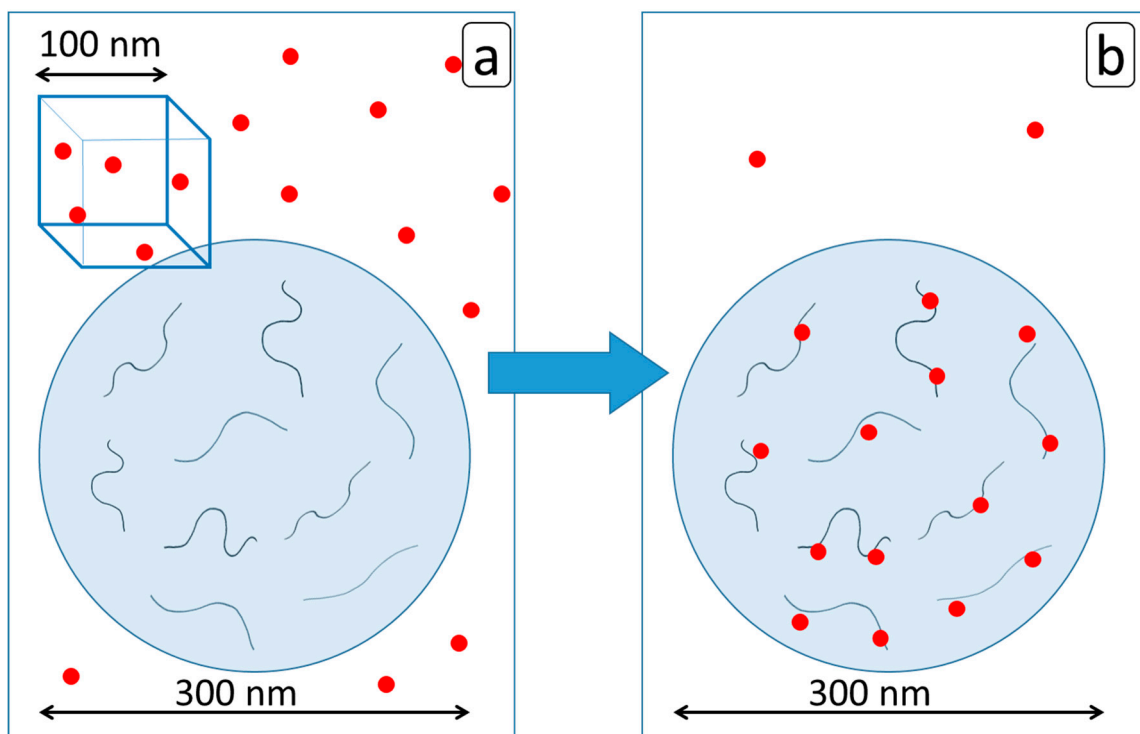
Figure 8. The proposed scheme of antiscalant efficacy due to sorption of solid impurities by aggregates of FAA-F1 molecules before (**a**) and after (**b**) the sorption takes place; red circles correspond to solids with the size of 1 nm, and blue ribbons correspond to PAA-F1 molecules (the size of solid impurities in the picture has been increased tenfold for better visibility, and the size of antiscalant has been increased three times).
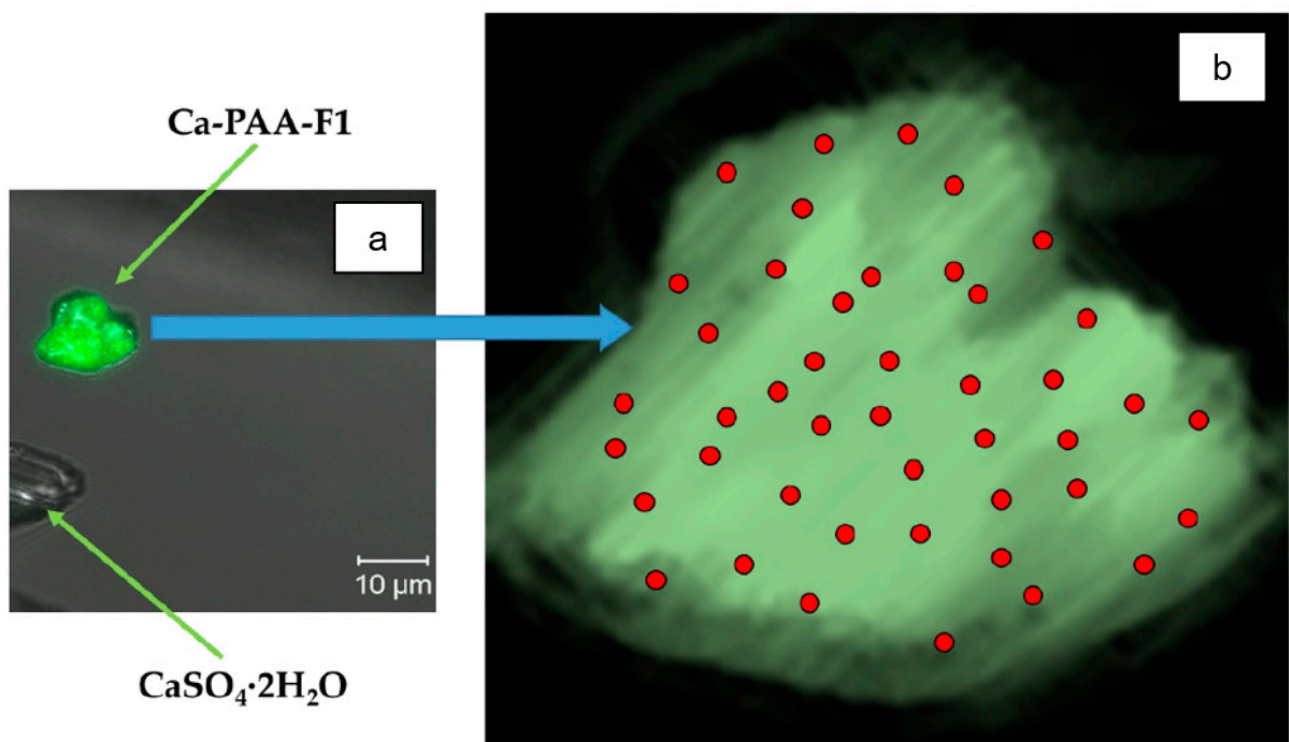

Figure 9. Two-dimensional fluorescence image of $CaSO_4 \cdot 2H_2O$ and Ca-PAA-F1 solids in the Ia experiment (**a**), and the proposed scheme of foreign nanoimpurities (indicated by red circles) accumulation by Ca-PAA-F1 particles (**b**).

Our results are inconsistent with the major tenets of classical nucleation theory (CNT) [53,54,81] and of the "non-classical" pre-nucleation cluster (PNC) pathway [82]. However, if a heterogeneous step of PNC adsorption by the solid nanoimpurity is assumed as an inevitable step of scale formation, and a competing process of solid nanoimpurity isolation from PNCs by antiscalant is considered, then the contradictions between our mechanism and the PNC pathway disappear. Thus, our interpretation of the inhibition of calcium sulfate deposition by PAA-F1 can be considered as a further refinement of the PNC pathway.

5. Conclusions

A paradoxical phenomenon of calcium sulfate deposition retardation in the presence of fluorescent-tagged polyacrylate PAA-F1 is described. Antiscalant causes a change in the crystal phase from bassanite to gypsum, significantly reduces the amount of precipitate, but does not show up at the kink, step, or selected edges of deposited crystals. Contrary to the predictions of the theory, it either remains in the aqueous phase, or forms its own separate phase Ca-PAA-F1.

It is demonstrated that the only scheme that allows one to explain the aforementioned paradox assumes that antiscalant does not block the surfaces of calcium sulfate nuclei or crystal surfaces, but rather the foreign particles of nanodust with particle sizes around 1 nm, naturally present in any aqueous solution. It is these particles that are responsible for nucleation and further growth of the deposit phase. Therefore, an antiscalant blocks these nanodust particles rather than the surface of sparingly soluble salt crystals. The number of calcium nucleation centers is then reduced, and the rate of scale formation decreases without any apparent antiscalant–scale interaction.

On the basis of the current experiment, the substoichiometric effect of scale inhibition obtained an alternative, quite a stoichiometric explanation. As a consequence, it is necessary to refine some theoretical foundations of scale inhibition.

The chemical and physical nature of nanodust is still unclear and difficult to quantify and analyze. Therefore, much work has to be conducted to gain insight into its properties. Alternatively, a strategy of combined action of flocculants, antiscalants, magnetic fields and ultrasound seems to be a matter of choice.

Author Contributions: Conceptualization, K.P. and M.O.; methodology, S.T., M.T. and A.R. (Anastasia Ryabova); validation, M.O.; software, A.R. (Anatoly Redchuk); validation, M.O.; formal analysis, A.R. (Anatoly Redchuk); investigation, M.O., M.T., A.R. (Anastasia Ryabova) and S.T.; resources, S.T.; data curation, A.R. (Anatoly Redchuk); writing—original draft preparation, K.P.; writing—review and editing, K.P. and S.T.; visualization, M.O.; supervision, M.O.; project administration, S.T.; funding acquisition, S.T. All authors have read and agreed to the published version of the manuscript.

References

1. Wang, M.; Cao, B.; Hu, Y.; Rodrigues, D.F. Mineral Scaling on Reverse Osmosis Membranes: Role of Mass, Orientation, and Crystallinity on Permeability. *Environ. Sci. Technol.* **2021**, *55*, 16110–16119. [CrossRef] [PubMed]
2. Dai, Z.; Zhao, Y.; Paudyal, S.; Wang, X.; Dai, C.; Ko, S.; Li, W.; Kan, A.T.; Tomson, M.B. Gypsum Scale Formation and Inhibition Kinetics with Implications in Membrane System. *Water Res.* **2022**, *225*, 119166. [CrossRef] [PubMed]
3. Yan, Z.; Lu, Z.; Chen, X.; Fan, G.; Qu, F.; Pang, H.; Liang, H. Integration of Seeding- and Heating-Induced Crystallization with Membrane Distillation for Membrane Gypsum Scaling and Wetting Control. *Desalination* **2021**, *511*, 115115. [CrossRef]
4. Todd, M.A.; Bluemle, M.J. Chapter 12—Formation and Mitigation of Mineral Scaling in Geothermal Power Plants. In *Water-Formed Deposits*; Amjad, Z., Demadis, K.D., Eds.; Elsevier: Amsterdam, The Netherlands, 2022; pp. 269–282; ISBN 978-0-12-822896-8.
5. Barber, M. Chapter 14—Recent Developments in Oilfield Scale Control. In *Water-Formed Deposits*; Amjad, Z., Demadis, K.D., Eds.; Elsevier: Amsterdam, The Netherlands, 2022; pp. 295–306; ISBN 978-0-12-822896-8.
6. Mady, M.F. Chapter 16—Oilfield Scale Inhibitors: Synthetic and Performance Aspects. In *Water-Formed Deposits*; Amjad, Z., Demadis, K.D., Eds.; Elsevier: Amsterdam, The Netherlands, 2022; pp. 325–352; ISBN 978-0-12-822896-8.
7. Yu, W.; Song, D.; Chen, W.; Yang, H. Antiscalants in RO Membrane Scaling Control. *Water Res.* **2020**, *183*, 115985. [CrossRef]
8. Liu, S.-T.; Nancollas, G.H. Linear Crystallization and Induction-Period Studies of the Growth of Calcium Sulphate Dihydrate Crystals. *Talanta* **1973**, *20*, 211–216. [CrossRef]
9. Packter, A. The Precipitation of Calcium Sulphate Dihydrate from Aqueous Solution: Induction Periods, Crystal Numbers and Final Size. *J. Cryst. Growth* **1974**, *21*, 191–194. [CrossRef]
10. Liu, S.-T.; Nancollas, G.H. The Kinetics of Crystal Growth of Calcium Sulfate Dihydrate. *J. Cryst. Growth* **1970**, *6*, 281–289. [CrossRef]
11. Nancollas, G.H.; Reddy, M.M.; Tsai, F. Calcium Sulfate Dihydrate Crystal Growth in Aqueous Solution at Elevated Temperatures. *J. Cryst. Growth* **1973**, *20*, 125–134. [CrossRef]
12. Nancollas, G.H.; Eralp, A.E.; Gill, J.S. Calcium Sulfate Scale Formation: A Kinetic Approach. *Soc. Pet. Eng. J.* **1978**, *18*, 133–138. [CrossRef]
13. Keller, D.M.; Massey, R.E.; Hileman, O.E., Jr. Studies on Nucleation Phenomena Occurring in Aqueous Solutions Supersaturated with Calcium Sulfate. *Can. J. Chem.* **1978**, *56*, 831–838. [CrossRef]
14. He, S.; Oddo, J.E.; Tomson, M.B. The Nucleation Kinetics of Calcium Sulfate Dihydrate in NaCl Solutions up to 6 m and 90 °C. *J. Colloid Interface Sci.* **1994**, *162*, 297–303. [CrossRef]
15. Ahmi, F.; Gadri, A. Kinetics and Morphology of Formed Gypsum. *Desalination* **2004**, *166*, 427–434. [CrossRef]
16. Linnikov, O.D. Investigation of the Initial Period of Sulphate Scale Formation Part 1. Kinetics and Mechanism of Calcium Sulphate Surface Nucleation at Its Crystallization on a Heat-Exchange Surface. *Desalination* **1999**, *122*, 1–14. [CrossRef]
17. Klepetsanis, P.G.; Dalas, E.; Koutsoukos, P.G. Role of Temperature in the Spontaneous Precipitation of Calcium Sulfate Dihydrate. *Langmuir* **1999**, *15*, 1534–1540. [CrossRef]
18. Prisciandaro, M.; Lancia, A.; Musmarra, D. Gypsum Nucleation into Sodium Chloride Solutions. *AIChE J.* **2001**, *47*, 929–934. [CrossRef]
19. Abdel-Aal, E.A.; Rashad, M.M.; El-Shall, H. Crystallization of Calcium Sulfate Dihydrate at Different Supersaturation Ratios and Different Free Sulfate Concentrations. *Cryst. Res. Technol.* **2004**, *39*, 313–321. [CrossRef]
20. Reiss, A.G.; Gavrieli, I.; Rosenberg, Y.O.; Reznik, I.J.; Luttge, A.; Emmanuel, S.; Ganor, J. Gypsum Precipitation under Saline Conditions: Thermodynamics, Kinetics, Morphology, and Size Distribution. *Minerals* **2021**, *11*, 141. [CrossRef]
21. Stawski, T.M.; van Driessche, A.E.S.; Ossorio, M.; Diego Rodriguez-Blanco, J.; Besselink, R.; Benning, L.G. Formation of Calcium Sulfate through the Aggregation of Sub-3 Nanometre Primary Species. *Nat. Commun.* **2016**, *7*, 11177. [CrossRef]
22. Ossorio, M.; Stawski, T.M.; Rodríguez-Blanco, J.D.; Sleutel, M.; García-Ruiz, J.M.; Benning, L.G.; Van Driessche, A.E.S. Physico-chemical and Additive Controls on the Multistep Precipitation Pathway of Gypsum. *Minerals* **2017**, *7*, 140. [CrossRef]
23. Stawski, T.M.; Besselink, R.; Chatzipanagis, K.; Hövelmann, J.; Benning, L.G.; Van Driessche, A.E.S. Nucleation Pathway of Calcium Sulfate Hemihydrate (Bassanite) from Solution: Implications for Calcium Sulfates on Mars. *J. Phys. Chem. C* **2020**, *124*, 8411–8422. [CrossRef]
24. Mbogoro, M.M.; Peruffo, M.; Adobes-Vidal, M.; Field, E.L.; O'Connell, M.A.; Unwin, P.R. Quantitative 3D Visualization of the Growth of Individual Gypsum Microcrystals: Effect of $Ca^{2+}:SO_4^{2-}$ Ratio on Kinetics and Crystal Morphology. *J. Phys. Chem. C* **2017**, *121*, 12726–12734. [CrossRef]
25. Van Driessche, A.E.S.; Stawski, T.M.; Kellermeier, M. Calcium Sulfate Precipitation Pathways in Natural and Engineered Environments. *Chem. Geol.* **2019**, *530*, 119274. [CrossRef]
26. Raju, K.; Atkinson, G.J. The thermodynamics of "Scale" mineral solubilities. 3. Calcium sulfate in aqueous sodium chloride. *J. Chem. Eng. Data* **1990**, *35*, 361–367. [CrossRef]
27. Anduix-Canto, C.; Levenstein, M.A.; Kim, Y.-Y.; Godinho, J.R.A.; Kulak, A.N.; Niño, C.G.; Withers, P.J.; Wright, J.P.; Kapur, N.; Christenson, H.K.; et al. Exploiting Confinement to Study the Crystallization Pathway of Calcium Sulfate. *Adv. Funct. Mater.* **2021**, *31*, 2107312. [CrossRef]
28. Ziegenheim, S.; Peintler, G.; Pálinkó, I.; Sipos, P. The Kinetics of the Precipitation of Gypsum, $CaSO_4 \cdot 2H_2O$, over a Wide Range of Reactant Concentrations. *React. Kinet. Mech. Catal.* **2020**, *131*, 75–88. [CrossRef]
29. Cao, T.; Rolf, J.; Wang, Z.; Violet, C.; Elimelech, M. Distinct Impacts of Natural Organic Matter and Colloidal Particles on Gypsum Crystallization. *Water Res.* **2022**, *218*, 118500. [CrossRef]

30. Hoang, T.A.; Ming Ang, H.M.; Rohl, A.L. Investigation into the effects of phosphonic inhibitors on the formation of calcium sulfate scales. *Desalin. Water Treat.* **2011**, *29*, 294–301. [CrossRef]

31. Jia, C.; Wu, L.; Fulton, J.L.; Liang, X.; De Yoreo, J.J.; Guan, B. Structural Characteristics of Amorphous Calcium Sulfate: Evidence to the Role of Water Molecules. *J. Phys. Chem. C* **2021**, *125*, 3415–3420. [CrossRef]

32. Amjad, Z. Applications of Antiscalants to Control Calcium Sulfate Scaling in Reverse Osmosis Systems. *Desalination* **1985**, *54*, 263–276. [CrossRef]

33. Amjad, Z. Kinetics of Crystal Growth of Calcium Sulfate Dihydrate. The Influence of Polymer Composition, Molecular Weight, and Solution pH. *Can. J. Chem.* **1988**, *66*, 1529–1536. [CrossRef]

34. Hasson, D.; Drak, A.; Semiat, R. Induction Times Induced in an RO System by Antiscalants Delaying CaSO$_4$ Precipitation. *Desalination* **2003**, *157*, 193–207. [CrossRef]

35. Lioliou, M.G.; Paraskeva, C.A.; Koutsoukos, P.G.; Payatakes, A.C. Calcium Sulfate Precipitation in the Presence of Water-Soluble Polymers. *J. Colloid Interface Sci.* **2006**, *303*, 164–170. [CrossRef] [PubMed]

36. Shih, W.-Y.; Gao, J.; Rahardianto, A.; Glater, J.; Cohen, Y.; Gabelich, C.J. Ranking of Antiscalant Performance for Gypsum Scale Suppression in the Presence of Residual Aluminum. *Desalination* **2006**, *196*, 280–292. [CrossRef]

37. Ben Ahmed, S.; Tlili, M.M.; Ben Amor, M. Influence of a Polyacrylate Antiscalant on Gypsum Nucleation and Growth. *Cryst. Res. Technol.* **2008**, *43*, 935–942. [CrossRef]

38. Akyol, E.; Öner, M.; Barouda, E.; Demadis, K.D. Systematic Structural Determinants of the Effects of Tetraphosphonates on Gypsum Crystallization. *Cryst. Growth Des.* **2009**, *9*, 5145–5154. [CrossRef]

39. Rosenberg, Y.O.; Reznik, I.J.; Zmora-Nahum, S.; Ganor, J. The Effect of pH on the Formation of a Gypsum Scale in the Presence of a Phosphonate Antiscalant. *Desalination* **2012**, *284*, 207–220. [CrossRef]

40. Rahman, F. Calcium Sulfate Precipitation Studies with Scale Inhibitors for Reverse Osmosis Desalination. *Desalination* **2013**, *319*, 79–84. [CrossRef]

41. Fan, C.; Kan, A.T.; Fu, G.; Tomson, M.B.; Shen, D. Quantitative Evaluation of Calcium Sulfate Precipitation Kinetics in the Presence and Absence of Scale Inhibitors. *SPE J.* **2010**, *15*, 977–988. [CrossRef]

42. Ali, S.A.; Kazi, I.W.; Rahman, F. Synthesis and Evaluation of Phosphate-Free Antiscalants to Control CaSO$_4\cdot$2H$_2$O Scale Formation in Reverse Osmosis Desalination Plants. *Desalination* **2015**, *357*, 36–44. [CrossRef]

43. Popov, K.; Rudakova, G.; Larchenko, V.; Tusheva, M.; Kamagurov, S.; Dikareva, J.; Kovaleva, N. A Comparative Performance Evaluation of Some Novel "Green" and Traditional Antiscalants in Calcium Sulfate Scaling. *Adv. Mater. Sci. Eng.* **2016**, *2016*, 7635329. [CrossRef]

44. Rabizadeh, T.; Morgan, D.J.; Peacock, C.L.; Benning, L.G. Effectiveness of Green Additives vs Poly(acrylic acid) in Inhibiting Calcium Sulfate Dihydrate Crystallization. *Ind. Eng. Chem. Res.* **2019**, *58*, 1561–1569. [CrossRef]

45. Prisciandaro, M.; Lancia, A.; Musmarra, D. Chapter 13—Gypsum Scale Control by Phosphonate Additives. In *Water-Formed Deposits*; Amjad, Z., Demadis, K.D., Eds.; Elsevier: Amsterdam, The Netherlands, 2022; pp. 283–294. ISBN 978-0-12-822896-8.

46. Cao, Z.; Hu, Y.; Zhao, H.; Cao, B.; Zhang, P. Sulfate Mineral Scaling: From Fundamental Mechanisms to Control Strategies. *Water Res.* **2022**, *222*, 118945. [CrossRef] [PubMed]

47. Benecke, J.; Rozova, J.; Ernst, M. Anti-scale effects of select organic macromolecules on gypsum bulk and surface crystallization during reverse osmosis desalination. *Sep. Purif. Technol.* **2018**, *198*, 68–78. [CrossRef]

48. Rabizadeh, T. Investigating the Potential of Hydroxyethylamino-di(methylene phosphonic acid) in Inhibiting Gypsum Crystallization. *CrystEngComm* **2023**, *25*, 935–944. [CrossRef]

49. Ziegenheim, S.; Sztegura, A.; Szabados, M.; Kónya, Z.; Kukovecz, Á.; Pálinkó, I.; Sipos, P. EDTA Analogues—Unconventional Inhibitors of Gypsum Precipitation. *J. Mol. Struct.* **2022**, *1256*, 132491. [CrossRef]

50. Gao, D.; Zhang, D.; Peng, Y.; Diao, H.; Wang, W. Effects of Different Carboxyl Additives on the Growth Habits of Hemihydrate Gypsum Crystals. *Constr. Build. Mater.* **2022**, *316*, 126037. [CrossRef]

51. Wang, Y.-W.; Kim, Y.-Y.; Christenson, H.K.; Meldrum, F.C. A New Precipitation Pathway for Calcium Sulfate Dihydrate (Gypsum) via Amorphous and Hemihydrate Intermediates. *Chem. Commun.* **2011**, *48*, 504–506. [CrossRef]

52. Mady, M.F.; Fevang, S.; Kelland, M.A. Study of Novel Aromatic Aminomethylenephosphonates as Oilfield Scale Inhibitors. *Energy Fuels* **2019**, *33*, 228–237. [CrossRef]

53. Mullin, J.W. *Crystallization*; Elsevier: Amsterdam, The Netherlands, 2001; ISBN 978-0-08-053011-6.

54. Kashchiev, D.; van Rosmalen, G.M. Review: Nucleation in Solutions Revisited. *Cryst. Res. Technol.* **2003**, *38*, 555–574. [CrossRef]

55. Hoang, T.A. Chapter 2—Mechanisms of Scale Formation and Inhibition. In *Water-Formed Deposits*; Amjad, Z., Demadis, K.D., Eds.; Elsevier: Amsterdam, The Netherlands, 2022; pp. 13–47. ISBN 978-0-12-822896-8.

56. Oshchepkov, M.S.; Popov, K.I. Chapter 35—Mechanisms of Scale Inhibition Derived from a Fluorescent-Tagged Antiscalant Visualization. In *Water-Formed Deposits*; Amjad, Z., Demadis, K.D., Eds.; Elsevier: Amsterdam, The Netherlands, 2022; pp. 765–782; ISBN 978-0-12-822896-8.

57. Zhang, Z.; Lu, M.; Liu, J.; Chen, H.; Chen, Q.; Wang, B. Fluorescent-Tagged Hyper-Branched Polyester for Inhibition of CaSO$_4$ Scale and the Scale Inhibition Mechanism. *Mater. Today Commun.* **2020**, *25*, 101359. [CrossRef]

58. Oshchepkov, M.; Kamagurov, S.; Tkachenko, S.; Ryabova, A.; Popov, K. Insight into the Mechanisms of Scale Inhibition: A Case Study of a Task-Specific Fluorescent-Tagged Scale Inhibitor Location on Gypsum Crystals. *ChemNanoMat* **2019**, *5*, 586–592. [CrossRef]

59. Oshchepkov, M.; Golovesov, V.; Ryabova, A.; Tkachenko, S.; Redchuk, A.; Rönkkömäki, H.; Rudakova, G.; Pervov, A.; Popov, K. Visualization of a Novel Fluorescent-Tagged Bisphosphonate Behavior during Reverse Osmosis Desalination of Water with High Sulfate Content. *Sep. Purif. Technol.* **2021**, *255*, 117382. [CrossRef]

60. Oshchepkov, M.; Golovesov, V.; Ryabova, A.; Frolova, S.; Tkachenko, S.; Kamagurov, S.; Rudakova, G.; Popov, K. Synthesis and Visualization of a Novel Fluorescent-Tagged Polymeric Antiscalant during Gypsum Crystallization in Combination with Bisphosphonate Fluorophore. *Crystals* **2020**, *10*, 992. [CrossRef]

61. Gil, V.; Oshchepkov, M.; Ryabova, A.; Trukhina, M.; Porozhnyy, M.; Tkachenko, S.; Pismenskaya, N.; Popov, K. Application and Visualization of Fluorescent-Tagged Antiscalants in Electrodialysis Processing of Aqueous Solutions Prone to Gypsum Scale Deposition. *Membranes* **2022**, *12*, 1002. [CrossRef] [PubMed]

62. Tkachenko, S.; Trukhina, M.; Ryabova, A.; Oshchepkov, M.; Kamagurov, S.; Popov, K. Fluorescent-Tagged Antiscalants—The New Materials for Scale Inhibition Mechanism Studies, Antiscalant Traceability and Antiscaling Efficacy Optimization during $CaCO_3$ and $CaSO_4 \cdot 2H_2O$ Scale Formation. *Int. J. Mol. Sci.* **2023**, *24*, 3087. [CrossRef] [PubMed]

63. Tkachenko, S.; Ryabova, A.; Oshchepkov, M.; Popov, K. Fluorescent-Tagged Antiscalants: A New Look at the Scale Inhibition Mechanism and Antiscalant Selection. *ChemNanoMat* **2022**, *8*, e202100370. [CrossRef]

64. Popov, K.; Oshchepkov, M.; Kamagurov, S.; Tkachenko, S.; Dikareva, J.; Rudakova, G. Synthesis and Properties of Novel Fluorescent-Tagged Polyacrylate-Based Scale Inhibitors. *J. Appl. Polym. Sci.* **2017**, *134*, 45017. [CrossRef]

65. *NACE Standard TM0374-2015, Item No. 21208*; Laboratory Screening Tests to Determine the Ability of Scale Inhibitors to Prevent the Precipitation of Calcium Sulfate and Calcium Carbonate from Solution (for Oil and Gas Production Systems). National Association of Corrosion Engineers: Houston, TX, USA, 2007.

66. Species. In *Solution Equilibria: Principles and Applications (for Windows 95, 98 and NT)*; Powell, K.J. (Ed.) Release 1; Academic Software: Otley, UK, 1999.

67. *Stability Constants Database and Mini-SCDatabase, version 5.3.*; IUPAC: Research Triangle Park, NC, USA; Academic Software: Otley, UK, 2011.

68. Korn, G.A.; Korn, T.M. *Mathematical Handbook for Scientists and Engineers: Definitions, Theorems, and Formulas for Reference and Review*; Courier Corporation: Chelmsford, MA, USA, 2000; ISBN 978-0-486-41147-7.

69. Wolfram Alpha LLC. Wolfram Alpha. 2023. Available online: https://www.wolframalpha.com/Input?I2d=true&i=Integrate%5BPower%5Bx%2C3%5DExp%5B-Power%5Bx%2C3%5D%5D%2C%7Bx%2C0%2C%E2%88%9E%7D%5D (accessed on 21 February 2023).

70. Marshall, W.L.; Slusher, R. Thermodynamics of Calcium Sulfate Dihydrate in Aqueous Sodium Chloride Solutions, 0–110°. *J. Phys. Chem.* **1966**, *70*, 4015–4027. [CrossRef]

71. Liu, X.; Sheng, X.; Yao, Q.; Zhao, L.; Xu, Z.; Zhou, Y. Synthesis of a New Type of 2-Phosphonobutane-1,2,4-tricarboxylic-acid-Modified Terpolymer Scale Inhibitor and Its Application in the Oil Field. *Energy Fuels* **2021**, *35*, 6136–6143. [CrossRef]

72. Liu, Y.; Zhou, Y.; Yao, Q.; Huang, J.; Liu, G.; Wang, H.; Cao, K.; Chen, Y.; Bu, Y.; Wu, W.; et al. Double-Hydrophilic Polyether Antiscalant Used as a Crystal Growth Modifier of Calcium Scales in Cooling-Water Systems. *J. Appl. Polym. Sci.* **2014**, *131*, 39792. [CrossRef]

73. Wang, H.; Zhou, Y.; Yao, Q.; Sun, W. Calcium Sulfate Precipitation Studies with Fluorescent-Tagged Scale Inhibitor for Cooling Water Systems. *Polym. Bull.* **2015**, *72*, 2171–2188. [CrossRef]

74. Middis, J.; Paul, S.T.; Müller-Stainhagen, H.M.; Duffy, G.G. Reduction of Heat Transfer Fouling by the Addition of Wood Pulp Fibers. *Heat Transf. Eng.* **1998**, *19*, 36–44. [CrossRef]

75. Duffy, G.G.; McShane, K.S. Heat-Transfer Fouling Mitigation with Model Synthetic Fibre Suspensions. *Asia-Pac. J. Chem. Eng.* **2007**, *2*, 407–412. [CrossRef]

76. Oshchepkov, M.; Popov, K.; Kovalenko, A.; Redchuk, A.; Dikareva, J.; Pochitalkina, I. Initial Stages of Gypsum Nucleation: The role of "Nano/microdust". *Minerals* **2020**, *10*, 1083. [CrossRef]

77. Trukhina, M.; Popov, K.; Oshchepkov, M.; Tkachenko, S.; Vorob'eva, A.; Rudakova, G. Impact of colloidal iron hydroxide and colloidal silicon dioxide on calcium sulfate crystallization in the presence of antiscalants. *Int. J. Corros. Scale Inhib.* **2022**, *11*, 1147–1171. [CrossRef]

78. Popov, K.; Oshchepkov, M.; Kovalenko, A.; Redchuk, A.; Dikareva, J.; Pochitalkina, I. Scale nucleation natural precursors: A case study of "micro/nanodust" impurities nature in laboratory aqueous samples obtained from Moscow tap water. *Int. J. Corros. Scale Inhib.* **2020**, *9*, 1097–1112. [CrossRef]

79. Aquilano, D.; Bruno, M.; Cotellucci, A.; Pastero, L.; Ghignone, S. Epitaxies of Ca-sulfates on calcite ($CaCO_3$) I. Gypsum {010} on the calcite {10.4} form: Epi-twins of gypsum induced by the calcite substrate. *CrystEngComm* **2022**, *24*, 5120–5127. [CrossRef]

80. Aquilano, D.; Bruno, M.; Ghignone, S.; Pasteroa, L.; Cotellucci, A. Epitaxies of Ca sulfates on calcite. II. The main {010}, {001} and {100} forms of bassanite epideposited on the {10.4} substrate form of calcite. *J. Appl. Cryst.* **2022**, *55*, 1289–1296. [CrossRef]

81. De Yoreo, J.J.; Vekilov, P.G. Principles of crystal nucleation and growth. *Rev. Mineral. Geochem.* **2003**, *54*, 57–93. [CrossRef]

82. Gebauer, D. How Can Additives Control the Early Stages of Mineralization? *Minerals* **2018**, *8*, 179. [CrossRef]